



# 1 Vortex Preconditioning of the 2021 Sudden Stratospheric Warming: 2 Barotropic/Baroclinic Instability Associated with the Double Westerly 3 Jets

4 Ji-Hee Yoo<sup>1</sup>, Hye-Yeong Chun<sup>1</sup>, Min-Jee Kang<sup>2</sup>

5 <sup>1</sup>Department of Atmospheric Sciences, Yonsei University, Seoul, 03722, South Korea

6 <sup>2</sup>School of Earth and Environmental Sciences, Seoul National University, Seoul, 08826, South Korea

7 Correspondence to: Hye-Yeong Chun (chunhy@yonsei.ac.kr)

8 **Abstract.** This study explores the abrupt split of the polar vortex in the upper stratosphere prior to a recent sudden  
9 stratospheric warming event on 5 January 2021 (SSW21) and the mechanisms of vortex preconditioning by using the  
10 Modern-Era Retrospective Analysis for Research and Applications version 2 (MERRA2) global reanalysis data. SSW21  
11 is preceded by the highly distorted polar vortex that was initially displaced off the pole but eventually split at the onset  
12 date. Vortex splitting is most significant in the mid-stratosphere (1 hPa altitude) accompanied by the anomalous growth  
13 of westward-propagating planetary waves (PWs) of zonal wavenumber (ZWN) 2 (WPW2). While previous studies have  
14 suggested the East Asian trough as a potential source for the abnormal WPW2 growth, the prominent westward-  
15 propagating nature cannot be explained satisfactorily by the upward propagation of the quasi-stationary ZWN2 fluxes  
16 in the troposphere. More importantly, WPW2 exhibits an obvious in-situ excitation signature within the barotropically  
17 and baroclinically destabilized stratosphere, dominated by the easterlies descending from the stratopause containing the  
18 WPW2 critical levels. This suggests that the vortex split is attributed to the WPW2 generated in situ within the  
19 stratosphere via instability. Vortex destabilization is achieved as the double-jet structure consisting of a subtropical  
20 mesospheric core and a polar stratospheric core develops into SSW21 by encouraging the anomalous dissipation of the  
21 upward-propagating tropospheric ZWN1 PWs. This double-jet configuration is likely a favorable precursor for SSW  
22 onset, not only for the SSW21 but generally for most SSWs, through promoting the anomalous growth of unstable PWs  
23 as well as the enhancement of the tropospheric PW dissipation.

24

## 25 1 Introduction

26 Sudden stratospheric warming (SSW) is a dramatic stratospheric phenomenon where the cold and strong westerly polar  
27 night jet (PNJ) rapidly decelerates or even reverses to easterly with an enormous warming within a week (Matsuno,  
28 1971). During SSW, the polar vortex is largely displaced away from the pole and/or split into two vortices (Charlton  
29 and Polvani, 2007, CP07). The impact of SSW is not limited to the polar stratosphere but extended into the mesosphere  
30 and above, causing significant changes in the residual circulations (Limpasuvan et al., 2016; Siskind et al., 2010), the  
31 distributions of chemical constituents such as ozone (Manney et al., 2009; Pedatella et al., 2018), and the atmospheric  
32 tides both in the Northern and Southern hemispheres. The dramatic temperature and wind perturbations during SSWs  
33 also descend into the troposphere, thereby altering the storm tracks which are closely tied to the surface weather patterns  
34 (Baldwin and Dunkerton, 2001; Hitchcock and Simpson, 2016).

35 SSW has been recognized as a manifestation of the interaction between the vertically propagating planetary waves (PWs)  
36 and stratospheric mean-flow. This is primarily driven by the upward-propagating anomalous tropospheric wave pulses,  
37 which can provide sufficient wave forcings to breakdown the polar vortex (Matsuno, 1971), and/or preconditioning of  
38 the stratosphere that focuses the tropospheric wave fluxes—not need to be anomalously strong—into the polar  
39 stratosphere (Birner and Albers, 2017; Palmer 1981). The preconditioning perspective has also been discussed in terms  
40 of the spontaneous wave explosion within the stratosphere (Plumb, 1981) as the polar vortex tunes itself toward the  
41 explosive wave-growth point, such as resonance (Albers and Birner, 2014, AB14) or barotropic/baroclinic (BT/BC)  
42 instability (Sato and Nomoto, 2015). Recent supports for the vortex preconditioning have been identified from  
43 observational (AB14; Iida et al., 2014) and modeling (Rhodes et al., 2021, RLO21) studies on the split-type SSW of  
44 January 2009 (SSW09). Such self-tuned SSWs are characterized by nearly instantaneous wave amplification throughout  
45 the entire stratosphere at the SSW onset. Within this context, AB14 interpreted the explosive growth of stratospheric  
46 wave activities as a manifestation of vortex breakdown, not the cause of SSW.

47 The latest major SSW took place on 5 January 2021 (SSW21), exhibiting the highly distorted polar vortex that was  
48 initially displaced off the pole but eventually split at the onset date. During the prewarming period, an initial zonal



49 wavenumber (ZWN) 1 pulse followed by a ZWN2 pulse was identified in the tropopause, suggesting their contributions  
50 to the observed vortex collapse (Cho et al., 2022; Lu et al., 2021; Rao et al., 2021). Lu et al. (2021) and Rao et al. (2021)  
51 related the intensification of the Aleutian low and the North Atlantic high in late December 2020 to the enhanced  
52 tropospheric ZWN1 flux and that of the East Asian trough developed in early January 2021 to the succeeding ZWN2  
53 flux. By performing numerical experiments, Cho et al. (2022) showed that the tropospheric ZWN1 pulse is attributed  
54 primarily to the North Pacific bomb cyclones that deepened the Aleutian low with a minor contribution from the Ural  
55 blocking.

56 This study expands upon previous research on SSW21 by examining the prewarming evolution of the vortex throughout  
57 the entire stratosphere, rather than solely in the region below 10 hPa conducted by most of previous studies on SSW21.  
58 We found that the most significant vortex split occurs in the mid-stratosphere (1 hPa). However, the anomalous  
59 stratospheric ZWN2 PWs (PW2) amplification responsible for this split cannot be explained by the concomitantly  
60 enhanced tropospheric ZWN2 fluxes. Therefore, this study explores vortex preconditioning in the context of the  
61 spontaneous PW2 explosion while addressing two questions: i) What is the source of the stratospheric PW2  
62 amplification? ii) How does the stratospheric vortex evolve toward the wave-growth point? To our knowledge, this is  
63 the first study to explore the role of vortex preconditioning in SSW21, providing more comprehensive accounts of the  
64 dynamics leading to SSW21.

65

## 66 **2 Data and Analysis Methods**

### 67 **2.1 The MERRA2 reanalysis data**

68 We use the Modern-Era Retrospective analysis for Research and Applications, version 2 (MERRA2) reanalysis data  
69 with a horizontal resolution of  $0.625^\circ \times 0.5^\circ$  (longitude  $\times$  latitude) and a temporal resolution of 3 hours from the surface  
70 to an altitude of 0.1 hPa (Gelaro et al., 2017) covering 42 years (1980–2021). All results in this study are based on the  
71 daily average.

72

### 73 **2.2 Analysis methods**

74 The Eliassen-Palm flux (EP-flux) and their divergence (EPFD), representing the wave activity flux and wave forcing,  
75 respectively, are calculated based on the following formulation (Andrews et al., 1987):

76

$$77 \quad \mathbf{F} = (F^\phi, F^z) = \rho_0 a \cos \phi \left( -\overline{u'v'} + \overline{u_z} \frac{\overline{v'\theta'}}{\theta_z}, \left[ f - \frac{1}{a \cos \phi} (\overline{u \cos \phi})_\phi \right] \frac{\overline{v'\theta'}}{\theta_z} - \overline{u'w'} \right), \quad (1)$$

$$78 \quad \nabla \cdot \mathbf{F} = \frac{1}{a \cos \phi} \frac{\partial}{\partial \phi} (F^\phi \cos \phi) + \frac{\partial F^z}{\partial z}, \quad (2)$$

79

80 where  $\phi$  and  $z$  are the latitude and log-pressure height, respectively,  $\rho_0$  is the reference density,  $a$  is the mean Earth's  
81 radius, and  $f$  is the Coriolis parameter.  $u$ ,  $v$ , and  $w$  are the zonal, meridional, and vertical wind components, respectively,  
82 and  $\theta$  is the potential temperature. The overbar and prime represent the zonal-mean and the departure from the zonal-  
83 mean, respectively.  $\mathbf{F}$  is the EP-flux vector, where  $F^\phi$  and  $F^z$  are the meridional and vertical components, respectively.  
84 EPFD corresponds to  $(1/\rho_0 a \cos \phi) \nabla \cdot \mathbf{F}$ .

85 BT/BC instability is evaluated by using the meridional gradient of the quasi-geostrophic potential vorticity (QGPV,  
86 Andrews et al., 1987):

87

$$88 \quad \overline{q}_y = \beta - \overline{u}_{yy} - \frac{1}{\rho_0} \left( \rho_0 \frac{f^2}{N^2} \overline{u_z} \right)_z, \quad (3)$$



89

90 where  $\bar{q}$ ,  $\beta$ , and  $N$  denote the zonal-mean QGPV, the meridional derivative of  $f$ , and the Brunt–Väisälä frequency,  
91 respectively. The necessary condition for BT/BC instability is that the generally positive  $\bar{q}_y$  associated with the  
92 wintertime circulation becomes negative (Salby, 1996). In Section 3, we refer to the sum of the first two terms on the  
93 right-hand side as the “barotropic term”, while the third term as “baroclinic term”.

94

### 95 **3 Results**

#### 96 **3.1 Wind and temperature changes during SSW21**

97 Figure 1a shows the time-evolutions of the zonal-mean zonal wind at 60°N and polar-cap temperature over 60–90°N  
98 during the development of SSW21. Remarkably, a reversal of the zonal-mean westerlies appears first in the lower  
99 mesosphere on 1 January and descends to 10 hPa within 4 days, leading to the onset of major SSW21 (CP07). It is  
100 preceded by the enormous deceleration of PNJ by ~108 m/s and a rapid 20 K warming in the mid-stratosphere (~1 hPa)  
101 within 8 days (28 December–4 January). Such a decrease (increase) in the zonal wind (temperature) is statistically  
102 significant at the 99% confidence level. Anomalous easterlies and warming descend into the troposphere and persist for  
103 longer than 20 days, which is much longer than the average persistence (~8 days) following SSWs in the reanalysis and  
104 CMIP models (Rao and Garfinkel, 2021).

105

#### 106 **3.2 Anomalous Enhancement of the Stratospheric PW2**

107 SSW21 is manifested by the polar vortex being severely displaced from the pole and ultimately split into two just before  
108 the onset. Associated PW activities are revealed in Figure 1b, which describes the time-evolutions of the geopotential  
109 height (GPH) amplitudes of PW1 and 2 at 60°N. As Lag = -1 is approached, the predominant PW1 amplitude drastically  
110 decreases, while the PW2 amplitude appreciably increases having the statistically significant positive anomaly at the  
111 95% confidence level at 1–3 hPa. From Lag = -2 to Lag = 1, PW2 dominates in the mid-to-upper stratosphere above 3  
112 hPa. Given the prevalent dominance of PW1 in the high-latitude winter stratosphere (Andrews et al., 1987; Matsuno  
113 1970), predominant PW2 activity observed in this case and other split-type SSWs is a notable feature. Evidenced in  
114 Figure 1c, which compares the polar-stereography series of the horizontal wind speed and the GPH anomaly at 1 and  
115 10 hPa, the vortex split is more pronounced in the mid-stratosphere than in the lower stratosphere, where PW1 have  
116 surpassed PW2 (Figure 1b).

117 Previous studies have suggested that the vortex split is attributed to the enhanced tropospheric ZWN2 fluxes entering  
118 the stratosphere, as evidenced by peak pulses of the ZWN2 eddy heat flux averaged over 45–75°N at 100 hPa during 1–  
119 5 January. However, this period nearly coincides with that of remarkable PW2 amplification in the mid-stratosphere  
120 (Figure 1b). This implies that the increased tropospheric fluxes must have instantaneously propagated up to ~28 km  
121 within the mid-to-upper stratosphere, which is highly questionable. Therefore, we examine whether the large  
122 tropospheric pulses are traceable to the upper stratosphere at the standard group velocity for vertically propagating PW2.  
123 Figure 2a illustrates the time-height cross section of the vertical component of EP-flux (EPFz) of PW2 in 45–75°N and  
124 the three identical vectors with a slope of 5.5 km/day, which corresponds to the theoretical group velocity of the  
125 vertically propagating Rossby waves of ZWN2 (Esler and Scott, 2005). For comparison purpose with previous studies,  
126 the time-series of eddy heat flux ( $\overline{v'T'}$ ) of ZWN1 and 2 in 45–75°N at 100 hPa are also presented below.

127 While  $\overline{v'T'}$  of ZWN1 reduces, that of ZWN2 increases from 28 December (Lag = -8), attaining a magnitude 1 STD  
128 greater than the climatology (but not significant) during 1–5 January. The theoretical prediction of Rossby waves’  
129 vertical propagation well matches the vertical propagation of EPFz below 5 hPa, indicating that the bulk of ZWN2  
130 fluxes propagate upward (AB14). However, as evidenced by the third vector, these waves could approach the upper  
131 stratosphere ~2 days after the onset date via upward propagation. This implies that the statistically significant PW2  
132 amplification in the upper stratosphere in Lag = -3–Lag = -1 (Figure 1b) cannot originate from the anomalous injection  
133 of the tropospheric wave activity during the same period.

134 More importantly, EPFz is not continuous above 5 hPa and exhibits apparent divergences with the downward EPFz  
135 (negative) below the region of upward EPFz (positive) around 3 hPa from Lag = -5 to Lag = -3. This suggests a potential  
136 for the in situ PW2 generation within the stratosphere. Despite the disappearance of downward EPFz after Lag = -2, the



137 divergence continues with the locally maximized upward EPFz in 10–3 hPa. In this view, subsequent statistically  
 138 significant enhancement in the upward EPFz (exceeding 99% confidence level) above the divergence altitude could be  
 139 a consequence of the upward propagation of the in situ generated PW2.

140 The evolution of the PW2 GPH in 45–75°N, as a function of zonal phase speed and time at the three altitudes depicted  
 141 in Figure 2b, supports this perspective. During the strengthening period of ZWN2  $\overline{v'T'}$  (Lag = -8–0), the tropospheric  
 142 PW2 (100 hPa) has a quasi-stationary nature, whereas the stratospheric PW2 (1–3 hPa) has prominent westward phase  
 143 speeds of 10–30 m/s (WPW2). The stratospheric WPW2 cannot be explained solely by the upward propagation of the  
 144 quasi-stationary tropospheric PWs.

145

### 146 3.3 In situ Source of the Stratospheric WPW2: BT/BC Instability

147 To examine the potential source of the stratospheric PW2, we first investigate EP-fluxes and EPFD of PW2 during the  
 148 WPW2 amplification period (1–5 January, Figure 3a). In this analysis, the overall PW2 behavior is investigated, not  
 149 exclusively for WPW2.

150 Throughout the period, significantly anomalous divergence of EP-fluxes (positive EPFD) appears, developing with the  
 151 rapidly intensifying easterlies. This demonstrates the spontaneous PW2 emanation within the stratosphere, which is  
 152 associated with the background flow: positive EPFD first appears between the easterlies extending from the equatorial  
 153 stratosphere and the polar jet core (Lag = -4). As the polar stratosphere becomes dominated by the descending  
 154 stratopause easterlies, the divergence is also enlarged towards 10 hPa and simultaneously intensified, exceeding 50  
 155 m/s/day at Lag = -2. While the easterlies further strengthen after that, the divergence area narrows below the jet core.  
 156 Nevertheless, the PW2 fluxes evolving along their propagation have magnitudes comparable to or even greater than the  
 157 previous ones. The upward propagating tropospheric fluxes, on the other hand, converge before reaching the easterlies,  
 158 imposing westward forcing. This is consistent with their quasi-stationary nature, which is inhibited by the zero-wind  
 159 line.

160 As a plausible in situ source for the stratospheric PW2, BT/BC instability is examined. Figures 3b–3d present the  
 161 latitude-height cross sections of  $\bar{q}_y$  and the barotropic and baroclinic terms of Equation (3), respectively. Negative  $\bar{q}_y$   
 162 satisfying the BT/BC instability condition emerges around the positive EPFD areas during the overall period. Similar to  
 163 the positive EPFD, this instability is exacerbated by the developing easterlies, attributed to both the barotropic and  
 164 baroclinic terms. The strengthening easterlies induce the positive  $\bar{u}_{yy}$  along their maxima, which dominates the positive  
 165  $\beta$ , leading to the vertically oriented negative barotropic term (Figure 3c). Concurrently, the baroclinic term becomes  
 166 negative from below the easterly core (Figure 3d). To elucidate the dominant factors that make the baroclinic term  
 167 negative, the third term of the right-hand side of Equation (3) is expanded as follows:

168

$$169 \quad -\frac{1}{\rho_0} \left( \rho_0 \frac{f^2}{N^2} \bar{u}_z \right)_z = f^2 \left[ \frac{1}{H} \frac{1}{N^2} \bar{u}_z + \frac{1}{N^4} \frac{dN^2}{dz} \bar{u}_z - \frac{1}{N^2} \bar{u}_{zz} \right], \quad (4)$$

170

171 where  $H$  is the scale height (7 km).

172 Figures 4a–4c present the latitude-height cross sections of the first, second, and third terms of the right-hand side of  
 173 Equation (4), respectively, divided by  $f^2$  during the vortex destabilization period (1–5 January). It shows that the  
 174 negative baroclinic term is attributed to both the first and third terms within the developing easterlies in the polar  
 175 stratosphere, with an insignificant compensation by positive value from the second term.

176 Figures 4d–4g show the latitude-height cross sections of the inverse of the squared Brunt–Väisälä frequency  $1/N^2$ , the  
 177 vertical gradient of the zonal-mean zonal wind  $\bar{u}_z$ , the vertical gradient of the Brunt–Väisälä frequency  $dN^2/dz$ , and  
 178 the vertical curvature of the zonal-mean zonal wind  $\bar{u}_{zz}$ , respectively, those consist of the three terms on Equation (4).  
 179 The negative first term is induced by the negative  $\bar{u}_z$  (Figure 4e) as the subtropical stratospheric easterlies propagate to  
 180 the polar stratopause (the polar stratopause easterlies descend into the lower stratosphere) on 1 January (2–5 January).  
 181 This negative  $\bar{u}_z$  along with the negative  $dN^2/dz$  (Figure 4f) makes the second term positive below the easterly jet core.  
 182 The negative third term, which is maximized above the easterly jet core, is caused by the strong positive  $\bar{u}_{zz}$  (Figure 4g)





183 under relatively small  $1/N^2$  (Figure 4e). Therefore, we conclude that the negative baroclinic term is attributed to the  
 184 negative  $\bar{u}_z$  (positive  $\bar{u}_{zz}$ ) below (centered at) the easterly jet core. Above findings suggest that the developing easterlies  
 185 cause WPW2 excitation by encouraging strong shear instabilities. These findings align with the numerical study by  
 186 Dickinson (1973): To serve instability as a source for PWs of a certain zonal phase speed  $C_x$ , the region must include a  
 187 critical layer where the zonal-mean zonal wind matches  $C_x$ . The presence of WPW2 critical levels near the in situ PW2  
 188 generation region is confirmed by the range of easterlies (-40–0 m/s) encompassing that of PW2's  $C_x$  in the mid-  
 189 stratosphere (1–3 hPa, Figure 2b). The collocation of negative  $\bar{q}_y$ , the emergent WPW2, and their critical levels  
 190 demonstrates that WPW2 grows by extracting energy from the unstable flow.

191 Yamazaki et al. (2021) found similar bursts of quasi-4-day WPW2s originating from the unstable stratosphere beyond  
 192 their critical level during the major SSWs in 2009, 2013, 2018, and 2019. Regarding the appearance of eastward-  
 193 propagating PWs of ZWN2 (EPW2) in the mesosphere before the SSW09 onset, Iida et al. (2014) also suspected in situ  
 194 generation via BT/BC instability in the westerly flow regime. RLO21 confirmed this possibility by identifying the  
 195 existence of the EPW2 critical level, but they interpreted EPW2 emergence as the over-reflection of the tropospheric  
 196 PW2 propagating upward. We explore the possibility of over-reflection for the amplified WPW2 by examining the  
 197 squared refractive index ( $n^2$ ):

198

$$199 \quad n^2 = \left[ \frac{\bar{q}_\phi}{a(\bar{u} - C_x)} - \left( \frac{k}{a \cos \phi} \right)^2 - \left( \frac{f}{2NH} \right)^2 \right] a^2. \quad (5)$$

200

201 Here, we set the zonal wavenumber  $k = 2$  and the zonal phase speed  $C_x = -10$  m/s, which corresponds to the identified  
 202 WPW2 peak in Figure 2b.

203 Figure 5 presents the latitude-height cross sections of the regions of negative  $\bar{q}_y$  and positive  $n^2$  with PW2 EP-fluxes  
 204 and EPFD in 1–5 January 2021. On 2 January, the over-reflection signal that bears a resemblance to the illustration in  
 205 Figure 1 in RLO21 is identified. Following the waveguide (orange hatched), the upward-propagating WPW2 are allowed  
 206 to reach the unstable region (mint shaded) where the critical level of WPW2 ( $C_x = -10$  m/s) is located. Leaving behind  
 207 a strong EP-flux divergence region, downward PW2 EP-flux vectors point away from the evanescent region of negative  
 208  $n^2$  (without orange hatched), which is formed by the negative  $\bar{q}_y$  and positive  $\bar{u} - C_x$ . These downward vectors can be  
 209 interpreted as the over-reflection of upward-propagating WPW2. This is consistent with the local downward EPFz below  
 210 the upward EPFz in Figure 2a. The positive  $n^2$  region associated with the transition from positive to negative  $\bar{u} - C_x$   
 211 under the negative  $\bar{q}_y$  from the evanescent region is suggestive of subsequent wave transmission. Transmitted waves  
 212 propagating from the critical layer can deposit their momentum, creating a region of EP-flux convergence (westward  
 213 acceleration). However, such over-reflection features become obscure from 3 January as the downward EPFz below the  
 214 evanescent region disappears. Moreover, the region of positive EPFD shifts to higher latitudes (60–90°N) than the region  
 215 where the upward-propagating WPW2 can reach (30–60°N). Therefore, the observed WPW2 amplification are not  
 216 satisfactorily explained through the over-reflection perspective.

217 Close inspection of the squared refractive index in Figure 5 also confirms that the wave resonance suggested by AB14  
 218 is less likely for the observed WPW2 explosion. Resonant wave events require a three-sided cavity of vertically  
 219 propagating PWs capable of trapping their energy. Such a cavity consists of two vertically oriented critical lines—one  
 220 in the midlatitudes and another in the polar regions—and a third horizontal one across the upper stratosphere. While  
 221 several localized regions of positive  $n^2$  exist within the instability areas, obvious features indicative of wave cavity are  
 222 not identified. Furthermore, the characteristic EPFz behavior indicating wave resonance, that is, vertically instantaneous  
 223 EPFz (AB14), is not identified in Figure 2a.

224 Alternately, Song et al. (2020) demonstrated that the mesospheric EPW2 was generated by the zonally asymmetric  
 225 gravity wave (GW) forcing, namely the non-conservative source term ( $Z'$ ) in the linearized perturbation QGPV equation.  
 226 We examine whether the rapid growth of the stratospheric WPW2 before the SSW21 onset is attributable to this  
 227 mechanism.

228 A linearized disturbance QGPV equation in log-pressure coordinates is as follows (Andrew et al., 1987):



229

$$230 \quad \left( \frac{\partial}{\partial t} + \bar{u} \frac{\partial}{a \cos \phi \partial \lambda} \right) q' + v' \frac{\partial \bar{q}}{a \partial \phi} = \frac{1}{a \cos \phi} \left[ \frac{\partial Y'}{\partial \lambda} - \frac{\partial (X' \cos \phi)}{\partial \phi} \right] + \frac{f_0}{\rho_0} \frac{\partial}{\partial z} \left[ \rho_0 \frac{e^{\frac{\kappa}{H} z}}{e^{\frac{\kappa}{H} z}} \left( \frac{\partial T_0}{\partial z} + \frac{\kappa T_0}{H} \right) \right], \quad (6)$$

$$231 \quad q' \equiv \frac{1}{a^2 \cos \phi} \left[ \frac{1}{\cos \phi} \frac{\partial^2}{\partial \lambda^2} + \frac{\partial}{\partial \phi} \left( \cos \phi \frac{\partial}{\partial \phi} \right) \right] \psi' + \frac{1}{\rho_0} \frac{\partial}{\partial z} \left( \rho_0 \frac{f_0^2}{N^2} \frac{\partial \psi'}{\partial z} \right), \quad (7)$$

$$232 \quad \frac{\partial \bar{q}}{a \partial \phi} \equiv \frac{2\Omega \cos \phi}{a} - \frac{1}{a^2} \frac{\partial}{\partial \phi} \left[ \frac{1}{\cos \phi} \frac{\partial (\bar{u} \cos \phi)}{\partial \phi} \right] - \frac{1}{\rho_0} \frac{\partial}{\partial z} \left( \rho_0 \frac{f_0^2}{N^2} \frac{\partial \bar{u}}{\partial z} \right). \quad (8)$$

233

234 Here,  $\lambda$  is the longitude, and  $q'$  is the QGPV perturbation.  $X'$  and  $Y'$  denote the perturbation of the zonal and meridional  
 235 components of GW forcing from their zonal-mean, respectively.  $Q'$  is the perturbation diabatic heating rate, and  $\psi'$  is  
 236 the perturbation streamfunction ( $\psi' = \phi'/f_0$ , where  $\phi'$  is the perturbation geopotential). The first bracketed term on the  
 237 right-hand side of Equation (6) is the nonconservative forcing term of the QGPV perturbation associated with the GW  
 238 drag (GWD). Therefore, we investigate whether the nonconservative GWD forcing defined by  $Z'$  below is related to the  
 239 rapid enhancement of WPW2 by using the zonal and meridional components of the parameterized GWD data  
 240 (McFarlane 1987; Molod et al., 2015).

241

$$242 \quad Z' = \frac{1}{a \cos \phi} \left[ \frac{\partial Y'}{\partial \lambda} - \frac{\partial (X' \cos \phi)}{\partial \phi} \right] \quad (9)$$

243

244 Figure 6a presents the latitude-height cross sections of the zonally averaged  $Z'$  magnitude ( $|Z'|$ ) and the positive EPFD  
 245 of PW2 during the amplification period of WPW2. The upward propagating parameterized GWs are dissipated in regions  
 246 with strong vertical shears of the zonal-mean zonal winds (see Figure S1), yielding the zonally asymmetric GW forcings.  
 247 Accordingly, the zonal-mean  $|Z'|$  is also identified above the strong shear region, where the positive EPFD is located.  
 248 However, due to the small magnitude of the GW forcing,  $|Z'|$  above the positive EPFD region (1–5 hPa) is much smaller  
 249 than  $|Z'|$  in the upper stratosphere and lower mesosphere (above 0.5 hPa), where  $Z'$  became significant enough to  
 250 generate EPW2 in Song et al. (2020). More importantly, as evidenced from a series of polar stereographic plots of  $Z'$   
 251 shown in Figure 6b, we cannot recognize an obvious ZWN2 structure. Therefore, we rule out the possibility of in situ  
 252 WPW2 generation driven by zonally asymmetric GW forcing as a nonconservative source of QGPV perturbation. Thus,  
 253 at least for the case of SSW21, our results support that BT/BC instability is the most likely source.

254

### 255 3.4 Vortex Preconditioning: Double Westerly Jets

256 The above findings lead us to examine the prewarming evolution of PNJ, which adjusts the vortex conducive to  
 257 instability. Figures 7a and 7b present the latitude-height cross sections of the zonal-mean zonal wind and the resolved  
 258 wave (RW) activities, respectively.

259 On 1–10 December 2020, the wind structure is similar to climatology, with a single maximum in the high-latitude  
 260 stratosphere. However, after the westerlies weaken over the following 10 days (11–20 December), the maximum moves  
 261 to the subtropical upper mesosphere (21–28 December). On 29 December, the wind structure largely deviates from the  
 262 climatology, consisting of two local maxima with comparable strength: one in the subtropical lower-mesosphere and the  
 263 other in the polar stratosphere. This so-called a double-jet configuration was also identified before the SSW09 onset  
 264 (Iida et al., 2014; RLO21). Along between the two maxima, the subtropical easterly progresses towards the polar  
 265 stratopause, which corresponds to a significant negative anomaly above the 95% confidence level. This abnormal



266 easterly completely separates the double-jets on 1 January, initiating shear instability (Figure 3b).

267 This is achieved through the critical-level interaction between the double westerly jets and RWs (Figure 7b). Around  
268 the zero-wind line between the subtropical easterly and the polar westerly, RWs propagating from the mid-latitude  
269 troposphere are critical-level filtered, exerting the statistically significant negative EPFD at the 99% confidence level.  
270 This negative forcing migrates the subtropical easterly poleward, further separating the jets. Subsequent RWs cannot  
271 propagate equatorward any further and are filtered within the poleward-shifted intervening region between the two jets,  
272 depositing again the anomalously strong negative forcing. The polar stratopause easterlies attributed to this positive  
273 feedback rapidly descend into 10 hPa and intensify dramatically beyond 80 m/s, causing exceptionally strong BT/BC  
274 instability. The negative RW forcing is mostly attributed to PW1 (Figure S2), whereas RWs having ZWN greater than  
275 1 contributed insignificantly or even counteracted (not shown).

276 In summary, vortex preconditioning for SSW21 is characterized by the double-jet configuration. By facilitating the  
277 critical-level interaction with the tropospheric PW1, this wind structure migrates the subtropical stratospheric easterlies  
278 into the polar stratopause, thereby initiating catastrophic vortex deceleration and adjusting the vortex toward explosive  
279 unstable PW2 growth.

280

### 281 **3.5 Destabilization of ZWN2 waves**

282 While the westward-propagating nature of the unstable PW2 is explained in connection with the background easterlies,  
283 it remains unclear why ZWN2 perturbations are predominantly amplified. One possibility is that the prevailing ZWN2  
284 fluxes forced from the troposphere may have been instantaneously destabilized at all altitudes, dominating over other  
285 waves. This speculation aligns with Hartmann's (1983) suggestion that predominant disturbances are more likely to be  
286 enhanced than those of higher ZWNs, despite their larger growth rates. However, it is not the case because the localized  
287 EPFz divergences in the stratosphere are decoupled from the troposphere (Figure 2a). Furthermore, the quasi-stationary  
288 tropospheric PW2 are not allowed to enter the stratosphere across their critical layer, as evidenced by their convergence  
289 near the zero-wind line (Figure 3a).

290 The more probable explanation is that WPW2 arise in situ within the destabilized stratosphere that nonlinearly interacts  
291 with PW1. Hartmann (1983) found that with the presence of PW1, the barotropic instability of PNJ could enhance the  
292 growth rates of shorter waves with similar phase speeds. Manney et al. (1991) identified similar destabilization of both  
293 waves 2 and 3, but wave 2 in particular. Relevant features are identified in Figure 8, which presents Ertel's PV (EPV)  
294 on the 1500 K isentropic surface (near 2 hPa). From 1 January, irreversible mixing associated with substantial PW1  
295 dissipation (Figure 7b) causes vortex filamentation along the vortex edge, yielding two additional high EPV cores.  
296 Concurrently, the initially localized negative EPV meridional gradient develops into a zonal-mean field, with the higher  
297 (lower) EPV advected toward the lower latitudes (pole). With growing instability, the two localized high EPV cores  
298 merge into one, exhibiting a ZWN2 pattern. Numerical experiments exploring the most unstable mode with respect to  
299 the given zonal flow can provide further convincing evidence, but that is beyond the scope of this study.

300

## 301 **4 Summary and Conclusion**

302 During the SSW21 onset, an anomalous WPW2 growth appears, which eventually splits the polar vortex. Previous  
303 studies have suggested that the enhanced ZWN2 fluxes originating from the tropospheric precursor events are  
304 responsible for this stimulating PW2 activities. However, simultaneous enhancements in PW2 activities in the  
305 tropopause and the mid-stratosphere are not explained solely by the vertical propagation of the tropospheric PW2. The  
306 prominent westward-propagating PW2 in the mid stratosphere that differs from the quasi-stationary tropospheric PW2  
307 complements this view.

308 This study demonstrates that the explosive WPW2 amplification occurs in situ within the polar stratosphere driven  
309 toward BT/BC instability, where the easterlies rapidly descend from the stratopause including the critical layer of WPW2.  
310 Vortex destabilization is induced as the abnormal double-jet structure having subtropical mesospheric and polar  
311 stratospheric cores evolves toward SSW21 within just 7 days. Therefore, we suggest vortex preconditioning for SSW21  
312 as the double-jet structure, which initiates vortex deceleration as well as tunes the vortex toward instability by facilitating  
313 the critical-level interaction with the tropospheric PWs.



314 Our findings provide some key insights into preconditioning of SSWs. First, vortex destabilization is an inevitable  
315 consequence of the zonal wind reversal to easterlies connected to the major SSWs. We found that all 26 major SSWs  
316 for 42 years (selected following the CP07 definition) exhibit BT/BC instability associated with the prevalent easterlies  
317 in the stratosphere at their onset (Figure S3). Given that an unstable flow supports the in situ PW explosion, which can  
318 even shape the vortex geometry shortly before the SSW onset, we suggest to look in more detail into the influences of  
319 BT/BC instability on the characteristics of SSW, including its onset, intensity, and duration. Second, the double-jets  
320 structure is likely a stratospheric precursor that favors triggering SSW. Approximately 70% (19) of 26 major SSWs  
321 exhibit this wind configuration within two weeks prior to their onset, despite variance in their occurrence timing (not  
322 shown). The present case SSW21 that occurred under unfavorable tropical conditions (the westerly quasi-biennial  
323 oscillation and weak convections) for SSW, reinforces this perspective. RLO21 also reported that this wind structure  
324 and associated unstable PW generation are commonly identified in other SSW events. Therefore, the preceding double-  
325 jets structure are worth examining in SSW studies to improve our understanding and predictability of SSWs. While this  
326 study focuses on the evolution of the double-jet structure toward SSW, it would also be fruitful to investigate the  
327 formation of such wind structure considering the interplay among PWs, GWs, and mean-flow (Iida et al., 2014; RLO21;  
328 Sato and Nomoto, 2015).

#### 329 **Data availability**

330 The MERRA2 data are available from the Global Modeling and Assimilation Office at NASA Goddard Space Flight  
331 Center through the NASA GES DISC online archive (available online at <https://doi.org/10.5067/WWQSQ8IVFW8>,  
332 GMAO, 2015). All results made in this study can be provided by the corresponding authors upon request.

#### 333 **Author contributions**

334 JHY, HYC, and MJK conceived the study. JHY conducted formal analysis and visualized the results. JHY wrote the  
335 draft with a contribution from HYC and MJK.

#### 336 **Competing interests**

337 The authors declare that they have no conflict of interest.

#### 338 **Financial support**

339 This work is supported by a National Research Foundation of Korea grant funded by the South Korea government (20  
340 21R1A2C100710212). The first author is supported by the Global PhD Fellowship Program (2019H1A2A1077307).

341

342



## 343 **References**

- 344 Albers, J. R. and Birner, T.: Vortex preconditioning due to planetary and gravity waves prior to sudden stratospheric warmings, J.  
345 Atmos. Sci., 71, 4028–4054, <https://doi.org/10.1175/JAS-D-14-0026.1>, 2014.
- 346 Andrews, D. G., Holton, J. R., and Leovy, C. B.: Middle atmosphere dynamics, 1st edn., vol. 40, edited by: Dmowska, R., and  
347 Holton, J. R., San Diego, Calif., Academic Press Inc, p. 489, ISBN: 9780120585762, 1987.
- 348 Baldwin, M. P., and Dunkerton, T. J.: Stratospheric harbingers of anomalous weather regimes. *Science*, 294, 581–584,  
349 <https://doi.org/10.1126/science.1063315>, 2001.
- 350 Birner, T. and Albers, J. R.: Sudden Stratospheric Warmings and Anomalous Upward Wave Activity Flux, *Scientific Online Letters*  
351 *on the Atmosphere*, 13, 8–12, <https://doi.org/10.2151/sola.13A-002>, 2017.
- 352 Charlton, A. J. and Polvani, L. M.: A New Look at Stratospheric Sudden Warmings. Part I: Climatology and Modeling Benchmarks,  
353 *J. Climate*, 20, 449–469, <https://doi.org/10.1175/JCLI3996.1>, 2007.
- 354 Cho, H. O., Kang, M. J., Son, S. W., Hong, D. C., and Kang, J. M.: A critical role of the North Pacific bomb cyclones in the onset  
355 of the 2021 sudden stratospheric warming, *Geophys. Res. Lett.*, 49,  
356 e2022GL099245, <https://doi.org/10.1029/2022GL099245>, 2022.
- 357 Dickinson, R. E.: Baroclinic instability of an unbounded zonal shear flow in a compressible atmosphere, *J. Atmos. Sci.*, 30, 1520–  
358 1527, [https://doi.org/10.1175/1520-0469\(1973\)030<1520:BIOAUZ>2.0.CO;2](https://doi.org/10.1175/1520-0469(1973)030<1520:BIOAUZ>2.0.CO;2), 1973.
- 359 Esler, J. G. and Scott, R. K.: Excitation of transient Rossby waves on the stratospheric polar vortex and the barotropic sudden  
360 warming, *J. Atmos. Sci.*, 62, 3661–3682, <https://doi.org/10.1175/JAS3557.1>, 2005.
- 361 Gelaro, R., McCarty, W., Suarez, M. J., Todling, R., Molod, A., Takacs, L., Randles, C. A., Darmenov, A., Bosilovich, M. G., Reichle,  
362 R., Wargan, K., Coy, L., Cullather, R., Draper, C., Akella, S., Buchard, V., Conaty, A., da Silva, A. M., Gu, W., Kim, G.-  
363 K., Koster, R., Lucchesi, R., Merkova, D., Nielsen, J. E., Partyka, G., Pawson, S., Putman, W., Rienecker, M., Schubert,  
364 S. D., Sienkiewicz, M., and Zhao, B.: The Modern-Era Retrospective Analysis for Research and Applications, Version 2  
365 (MERRA-2), *J. Climate*, 30, 5419–5454, <https://doi.org/10.1175/JCLI-D-16-0758.1>, 2017.
- 366 Hartmann, D. L.: Barotropic instability of the polar night jet stream, *J. Atmos. Sci.*, 40, 817–835, [https://doi.org/10.1175/1520-0469\(1983\)040<0817:BIOTPN>2.0.CO;2](https://doi.org/10.1175/1520-0469(1983)040<0817:BIOTPN>2.0.CO;2), 1983.
- 368 Hitchcock, P. and Simpson, I. R.: Quantifying eddy feedbacks and forcings in the tropospheric response to stratospheric sudden  
369 warmings, *J. Atmos. Sci.*, 73, 3641–3657, <https://doi.org/10.1175/JAS-D-16-0056.1>, 2016.
- 370 Iida, C., Hirooka, T., and Eguchi, N.: Circulation changes in the stratosphere and mesosphere during the stratospheric sudden  
371 warming event in January 2009, *J. Geophys. Res.-Atmos.*, 119, 7104–7115, <https://doi.org/10.1002/2013JD021252>, 2014.
- 372 Limpasuvan, V., Orsolini, Y. J., Chandran, A., Garcia, R. R., and Smith, A. K.: On the composite response of the MLT to major  
373 sudden stratospheric warming events with elevated stratopause, *J. Geophys. Res.-Atmos.*, 121, 4518–4537,  
374 <https://doi.org/10.1002/2015JD024401>, 2016.
- 375 Lu, Q., Rao, J., Liang, Z., Guo, D., Luo, J., Liu, S., Wang, C., and Wang, T.: The sudden stratospheric warming in January  
376 2021, *Environ. Res. Lett.*, 16, 084029, <https://doi.org/10.1088/1748-9326/ac12f4>, 2021.
- 377 Manney, G. L., Elson, L. S., Mecho, C. R., and Farrara, J. D.: Planetary-scale waves in the Southern Hemisphere winter and early  
378 spring stratosphere: Stability analysis, *J. Atmos. Sci.*, 48, 2509–2523, <https://doi.org/10.1175/1520->



- 379 0469(1991)048<2509:PSWITS>2.0.CO;2, 1991.
- 380 Manney, G. L., Schwartz, M. J., Krüger, K., Santee, M. L., Pawson, S., Lee, J. N., Daffer, W. H., Fuller, R. A., and Livesey, N. J.:  
381 Aura Microwave Limb Sounder observations of dynamics and transport during the record-breaking 2009 Arctic  
382 stratospheric major warming, *Geophys. Res. Lett.*, 36, <https://doi.org/10.1029/2009GL038586>, 2009.
- 383 Matsuno, T.: Vertical Propagation of Stationary Planetary Waves in the Winter Northern Hemisphere, *J. Atmos. Sci.*, 27, 871–883,  
384 [https://doi.org/10.1175/1520-0469\(1970\)027<0871:VPOSPW>2.0.CO;2](https://doi.org/10.1175/1520-0469(1970)027<0871:VPOSPW>2.0.CO;2), 1970.
- 385 Matsuno, T.: A dynamical model of the stratospheric sudden warming, *J. Atmos. Sci.*, 28, 1479–1494, [https://doi.org/10.1175/1520-0469\(1971\)028<1479:ADMOTS>2.0.CO;2](https://doi.org/10.1175/1520-0469(1971)028<1479:ADMOTS>2.0.CO;2), 1971.
- 387 McFarlane, N. A.: The effect of orographically excited gravity wave drag on the general circulation of the lower stratosphere and  
388 troposphere, *J. Atmos. Sci.*, 44, 1775–1800, [https://doi.org/10.1175/1520-0469\(1987\)044<1775:TEOOEG>2.0.CO;2](https://doi.org/10.1175/1520-0469(1987)044<1775:TEOOEG>2.0.CO;2),  
389 1987.
- 390 Molod, A., Takacs, L., Suarez, M., and Bacmeister, J.: Development of the GEOS-5 atmospheric general circulation model:  
391 evolution from MERRA to MERRA2, *Geosci. Model Dev.*, 8, 1339–1356, <https://doi.org/10.5194/gmd-8-1339-2015>,  
392 2015.
- 393 Palmer, T. N.: Aspects of stratospheric sudden warmings studied from a transformed Eulerian-mean viewpoint, *J. Geophys. Res.*,  
394 86, 9679–9687, <https://doi.org/10.1029/JC086iC10p09679>, 1981.
- 395 Pedatella, N. M., Liu, H.-L., Marsh, D. R., Raeder, K., Anderson, J. L., Chau, J. L., Goncharenko, L. P., and Siddiqui, T. A.: Analysis  
396 and hindcast experiments of the 2009 sudden stratospheric warming in WACCMX+DART, *J. Geophys. Res.-Space*, 123,  
397 3131–3153, <https://doi.org/10.1002/2017JA025107>, 2018.
- 398 Plumb, R. A.: Instability of the distorted polar night vortex: A theory of stratospheric warmings, *J. Atmos. Sci.*, 38, 2514–2531,  
399 [https://doi.org/10.1175/1520-0469\(1981\)038<2514:IOTDPN>2.0.CO;2](https://doi.org/10.1175/1520-0469(1981)038<2514:IOTDPN>2.0.CO;2), 1981.
- 400 Rao, J., Garfinkel, C. I., Wu, T., Lu, Y., Lu, Q., and Liang, Z.: The January 2021 sudden stratospheric warming and its prediction in  
401 subseasonal to seasonal models, *J. Geophys. Res.-Atmos.*, 126, e2021JD035057, <https://doi.org/10.1029/2021JD035057>,  
402 2021.
- 403 Rao, J. and Garfinkel, C. I.: CMIP5/6 Models Project Little Change in the Statistical Characteristics of Sudden Stratospheric  
404 Warmings in the 21st Century, *Environ. Res. Lett.*, 16, 034024, <https://doi.org/10.1088/1748-9326/abd4fe>, 2021.
- 405 Rhodes, C. T., Limpasuvan, V., and Orsolini, Y. J.: Eastward-propagating planetary waves prior to the January 2009 sudden  
406 stratospheric warming, *J. Geophys. Res.-Atmos.*, 126, e2020JD033696, <https://doi.org/10.1029/2020JD033696>, 2021.
- 407 Salby, M. L.: Fundamentals of atmospheric physics, no. v. 61 in International geophysics series, Academic Press, San Diego, 648  
408 pp., ISBN 9780080532158, 1996.
- 409 Sato, K., and Nomoto, M.: Gravity wave–induced anomalous potential vorticity gradient generating planetary waves in the winter  
410 mesosphere, *J. Atmos. Sci.*, 72, 3609–3624, <https://doi.org/10.1175/JAS-D-15-0046.1>, 2015.
- 411 Siskind, D. E., Eckeremann, S. D., McCormack, J. P., Coy, L., Hoppel, K.W., and Baker, N. L.: Case studies of the mesospheric  
412 response to recent minor, major, and extended stratospheric warmings, *J. Geophys. Res.*, 115, D00N03,  
413 <https://doi.org/10.1029/2010JD014114>, 2010.
- 414 Song, B. G., Chun, H. Y., and Song, I. S.: Role of gravity waves in a vortex-split sudden stratospheric warming in January 2009, *J.*  
415 *Atmos. Sci.*, 77, 3321–3342, <https://doi.org/10.1175/JAS-D-20-0039.1>, 2020.



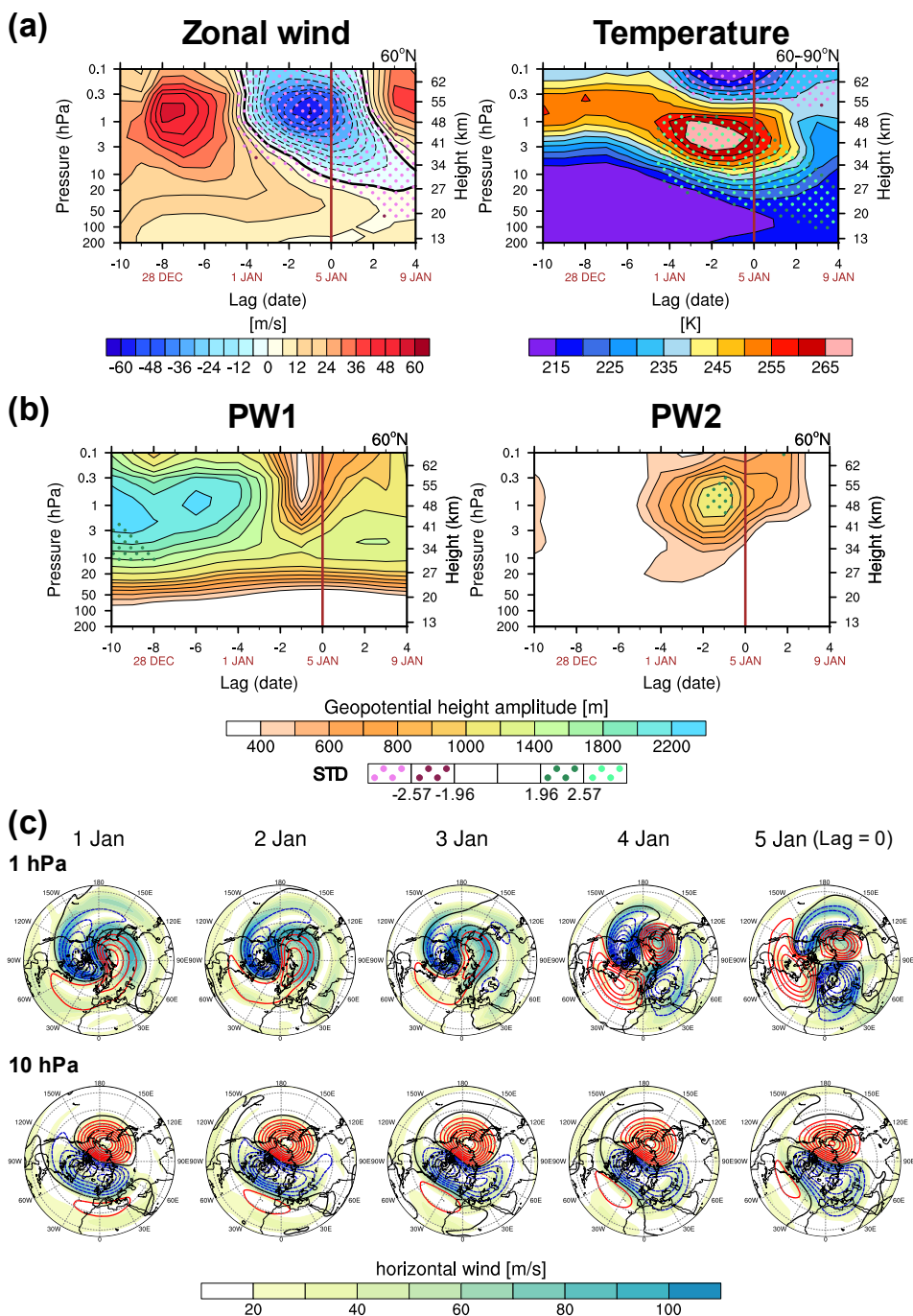
<https://doi.org/10.5194/egusphere-2023-1044>

Preprint. Discussion started: 5 June 2023

© Author(s) 2023. CC BY 4.0 License.

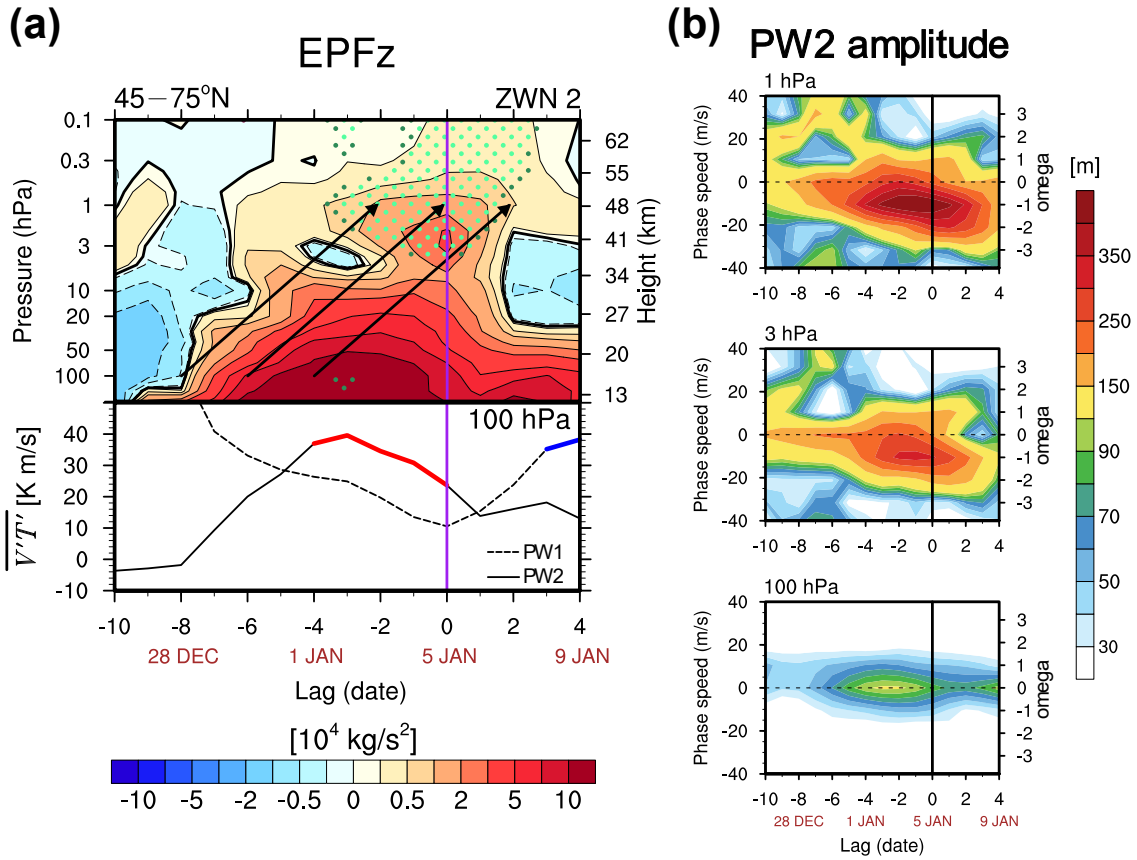


416 Yamazaki, Y., Matthias, V., and Miyoshi, Y.: Quasi-4-Day Wave: Atmospheric Manifestation of the First Symmetric Rossby Normal  
417 Mode of Zonal Wavenumber 2, *J. Geophys. Res.-Atmos.*, 126, e2021JD034855, <https://doi.org/10.1029/2021JD034855>,  
418 2021.



419

420 **Figure 1:** Time-height cross sections of (a) the zonal-mean zonal wind at 60°N (left) and polar cap temperature averaged  
 421 over 60–90°N (right) and (b) the geopotential height (GPH) amplitude of the planetary waves (PWs) with zonal  
 422 wavenumbers (ZWN) 1 (PW1, left) and 2 (PW2, right) at 60°N. The dark and bright pink (green) dots denote regions  
 423 where the analyzed variable is algebraically smaller (larger) than its 42-year climatology by more than 1.96 and 2.57  
 424 standard deviations (STD), indicating that the variable is significantly anomalous at the 95 and 99% confidence levels,  
 425 respectively. (c) Polar stereography series of the horizontal wind speed (shading) and GPH anomalies from their zonal-  
 426 mean (contours) at 1 hPa (upper) and 10 hPa (lower) on 1–5 January. The red (blue) contour represents the positive  
 427 (negative) value.



428

429 **Figure 2:** (a) Time-height cross sections of the vertical component of Eliassen-Palm fluxes (EPFz) of PW2 (upper) and  
 430 time-series of eddy heat flux ( $\overline{v'T'}$ ) of PW1 (dashed) and PW2 (solid) at 100 hPa (lower) averaged over 45–75°N. The  
 431 overlaid blue (red) thick line denotes  $\overline{v'T'}$  of PW1 (PW2) having a magnitude 1 STD greater than its climatology. (b)  
 432 Time-zonal phase speed cross sections of the PW2 GHP amplitude at 1, 3, and 100 hPa averaged over 45–75°N. The  
 433 purple and black vertical lines in (a) and (b), respectively, represent the onset date.

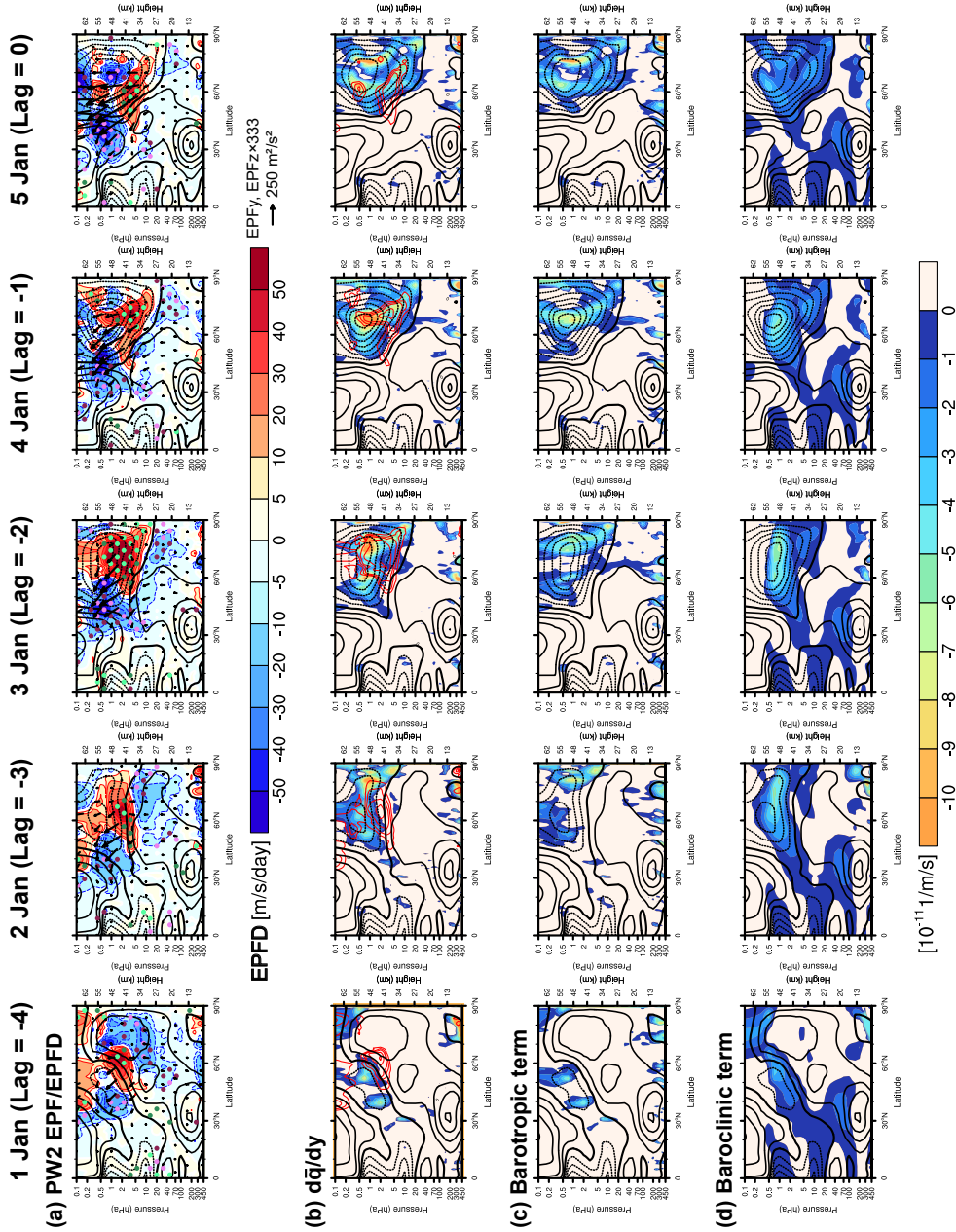


**Figure 3:** Latitude-height cross sections of (a) Eliassen-Palm fluxes (EPF-fluxes, vectors) overlaid on their divergences (EPFD, colors) of PW2, (b) the meridional gradient of the quasi-geostrophic potential vorticity ( $\bar{q}_y$ , colors) overlaid by the positive EPFD of PW2 (red contour), (c) barotropic, and (d) baroclinic terms of Equation (3) in 1–5 January. The black contours present the zonal-mean zonal winds. The solid, dashed, and thick solid lines indicate positive, negative, and zero wind, respectively.



5 Jan (Lag = 0)

4 Jan (Lag = -1)

3 Jan (Lag = -2)

2 Jan (Lag = -3)

1 Jan (Lag = -4)

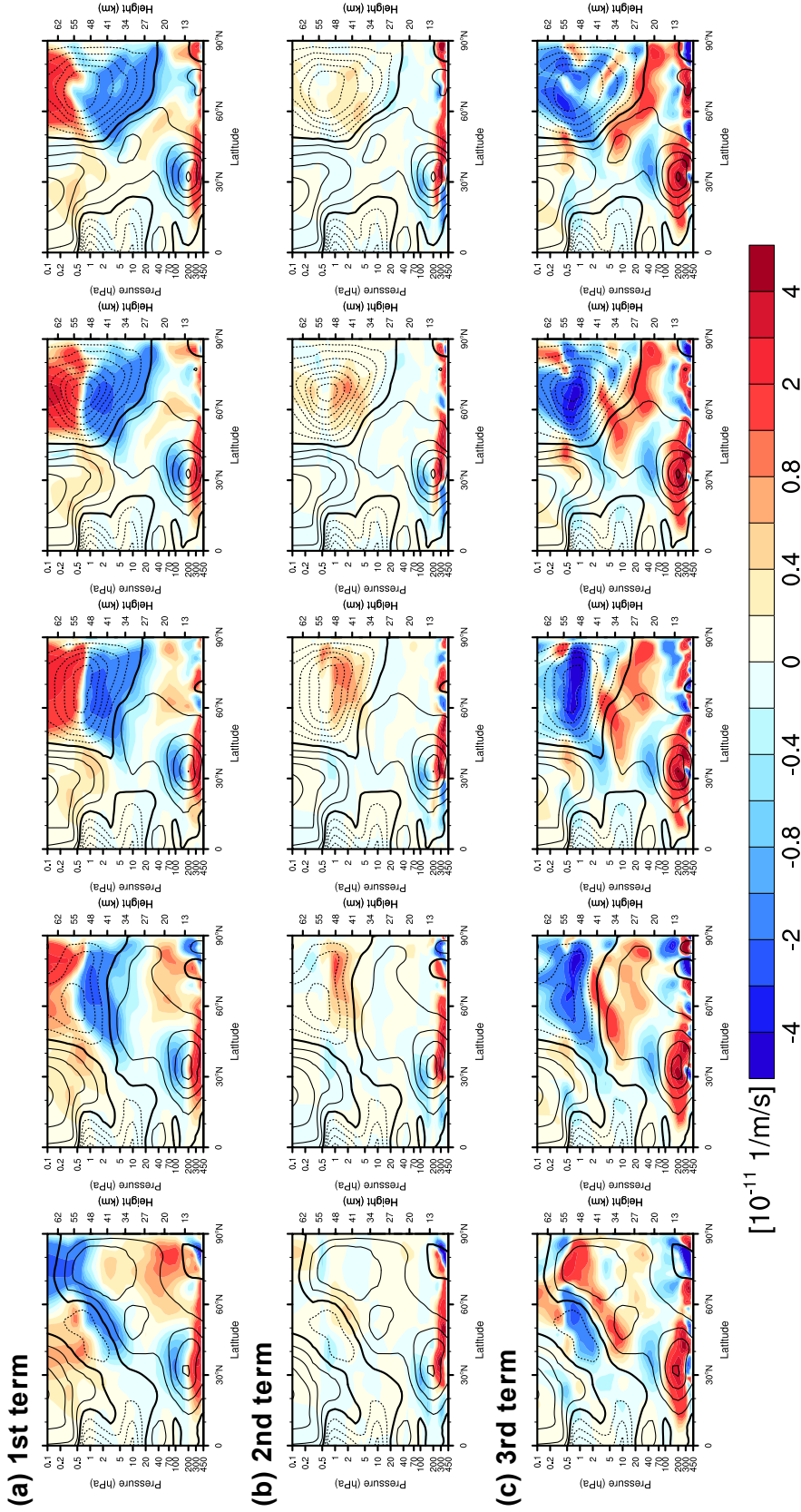


**Figure 4:** Latitude-height cross sections of (a–c) the three terms on the right-hand side of Equation (4) divided by  $f^2$ , (d) the inverse of the squared Brunt–Väisälä frequency  $\frac{1}{N^2}$ , (e) the vertical gradient of the squared Brunt–Väisälä frequency  $N^2_z$ , and (g) the vertical curvature of the zonal-mean zonal wind  $\bar{u}_{zz}$  on 1–5 January 2021. The black contours present the zonal-mean zonal winds. The solid, dashed, and thick solid lines denote positive, negative, and zero wind, respectively.



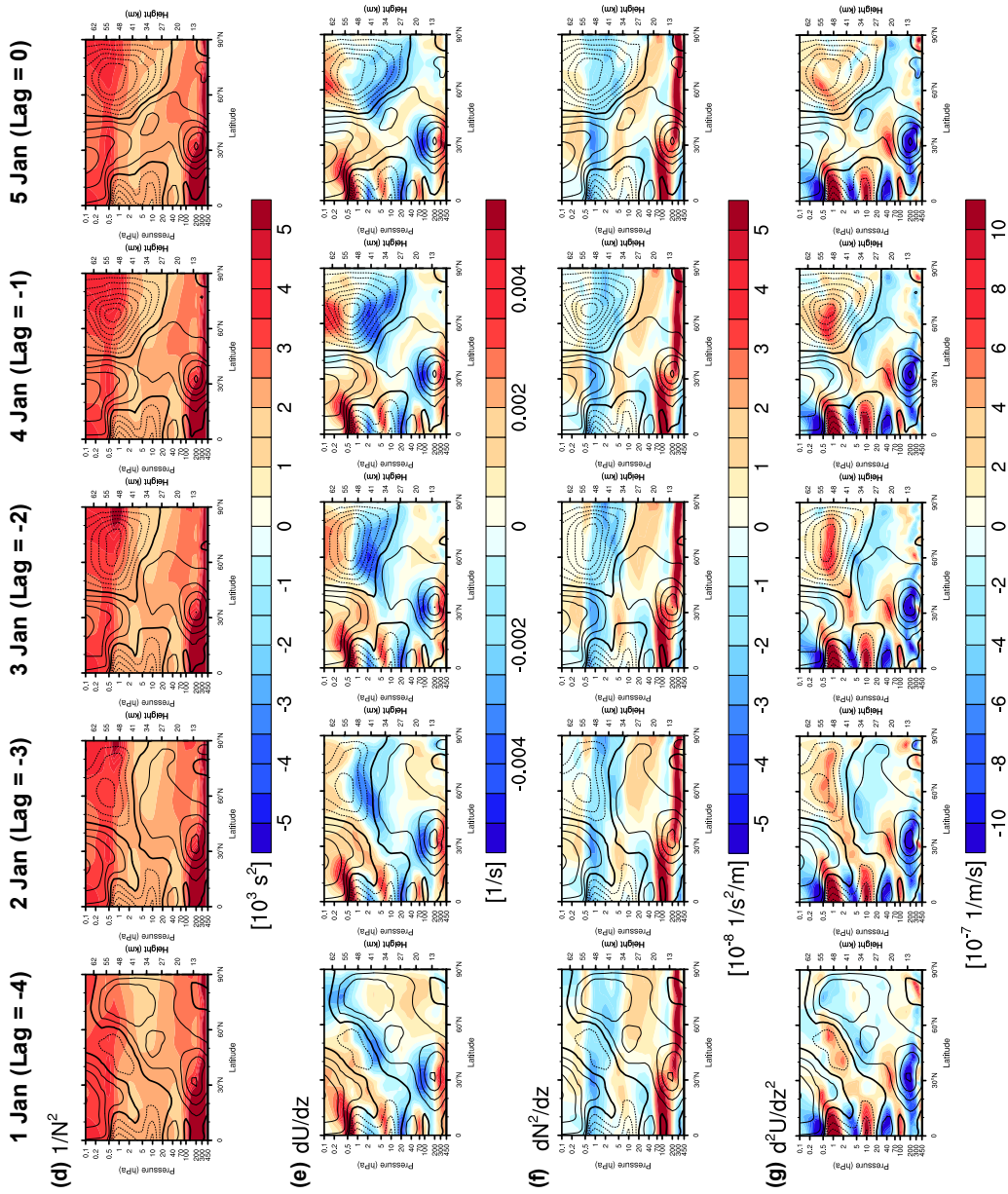
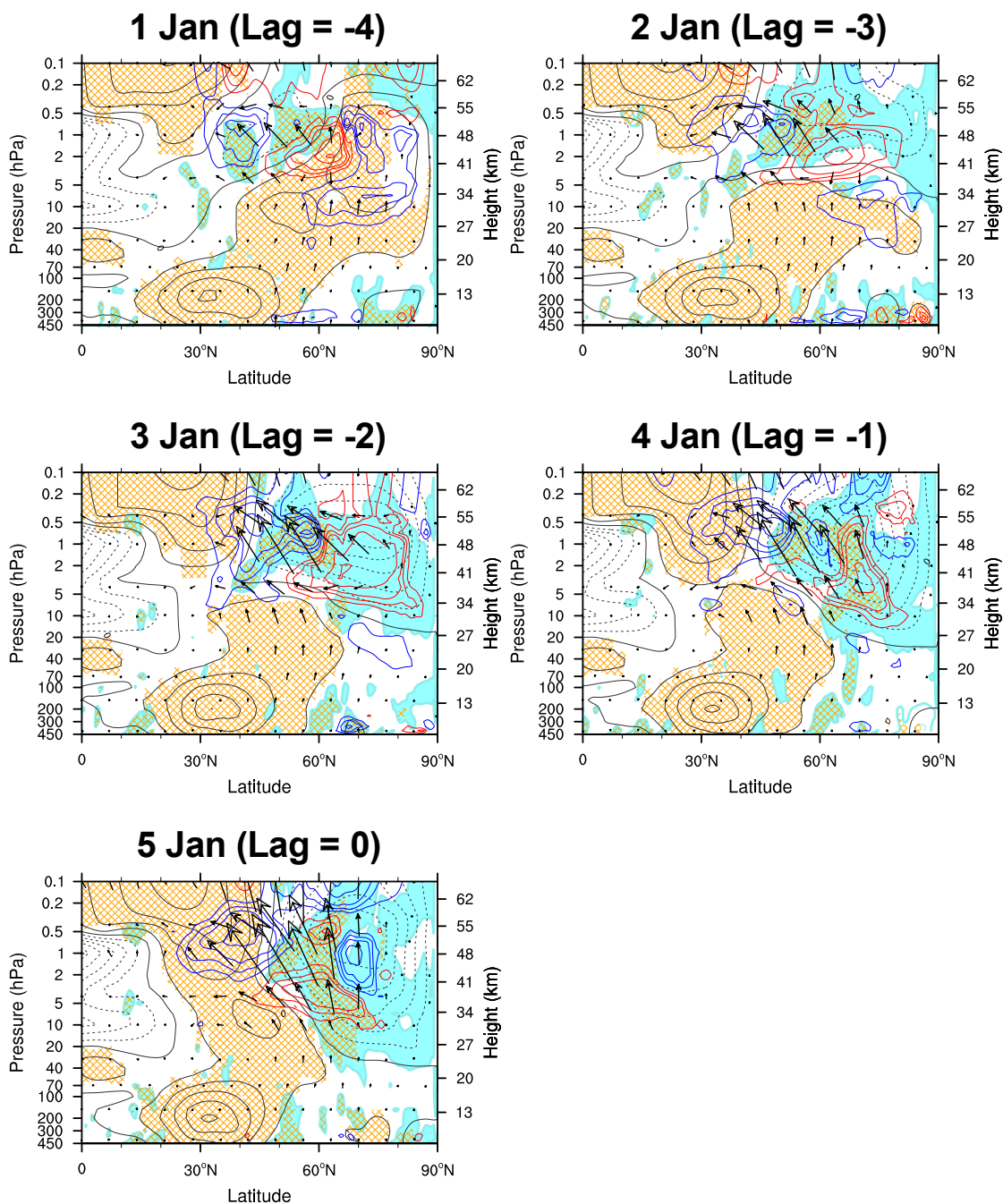


Figure 4: (Continued).





445

446 **Figure 5:** Latitude-height cross sections of the negative  $\bar{q}_y$ , (mint shading) and positive refractive index squared ( $n^2$ ,  
 447 orange hatching) overlaid by PW2 EP-fluxes (vectors) and EPFD (contours, where the red and blue contours denote the  
 448 positive and negative values, respectively) in 1–5 January 2021. The black contours present the zonal-mean zonal winds.  
 449 The solid, dashed, and thick solid lines denote positive, negative, and zero wind, respectively.

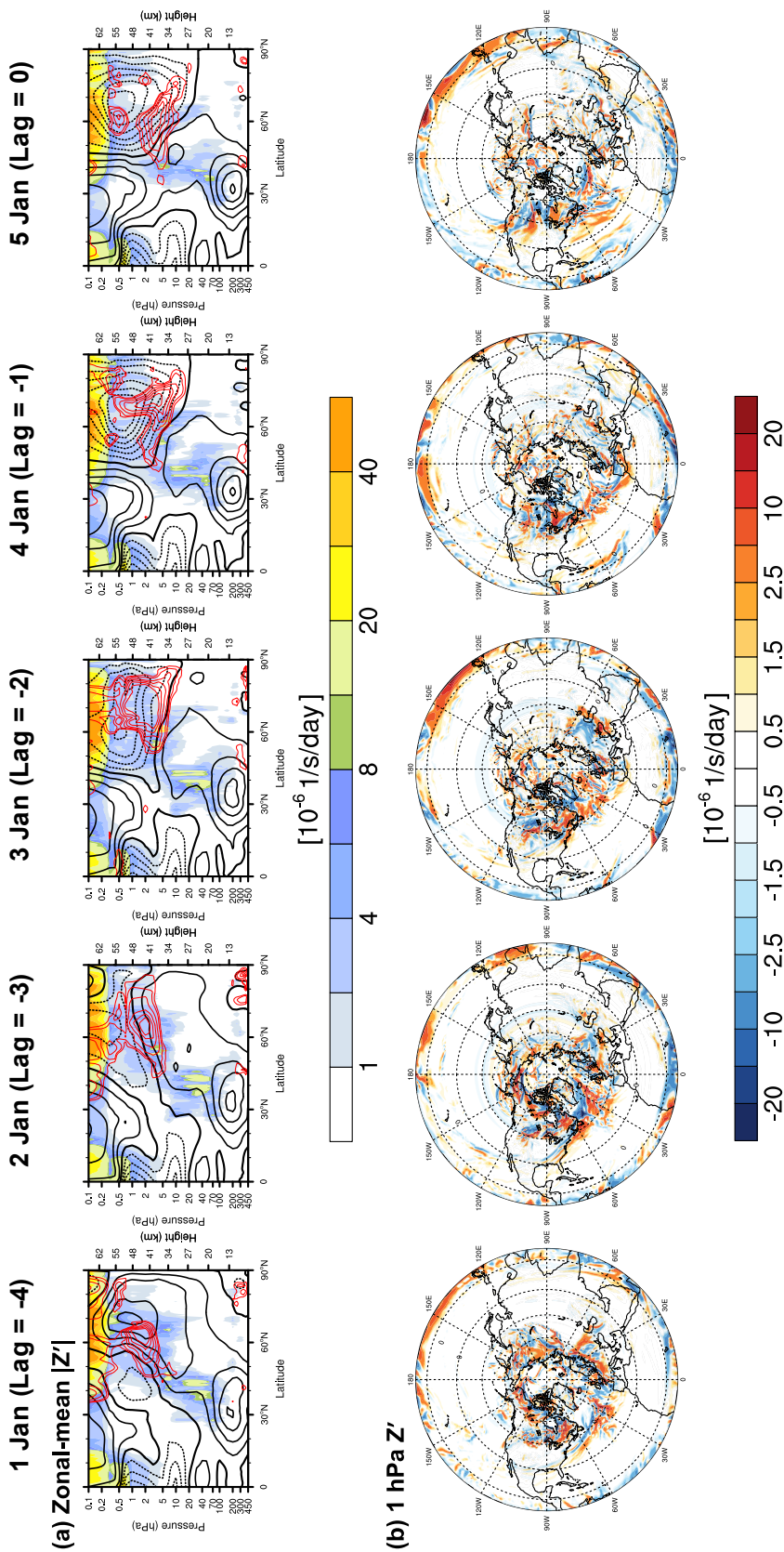
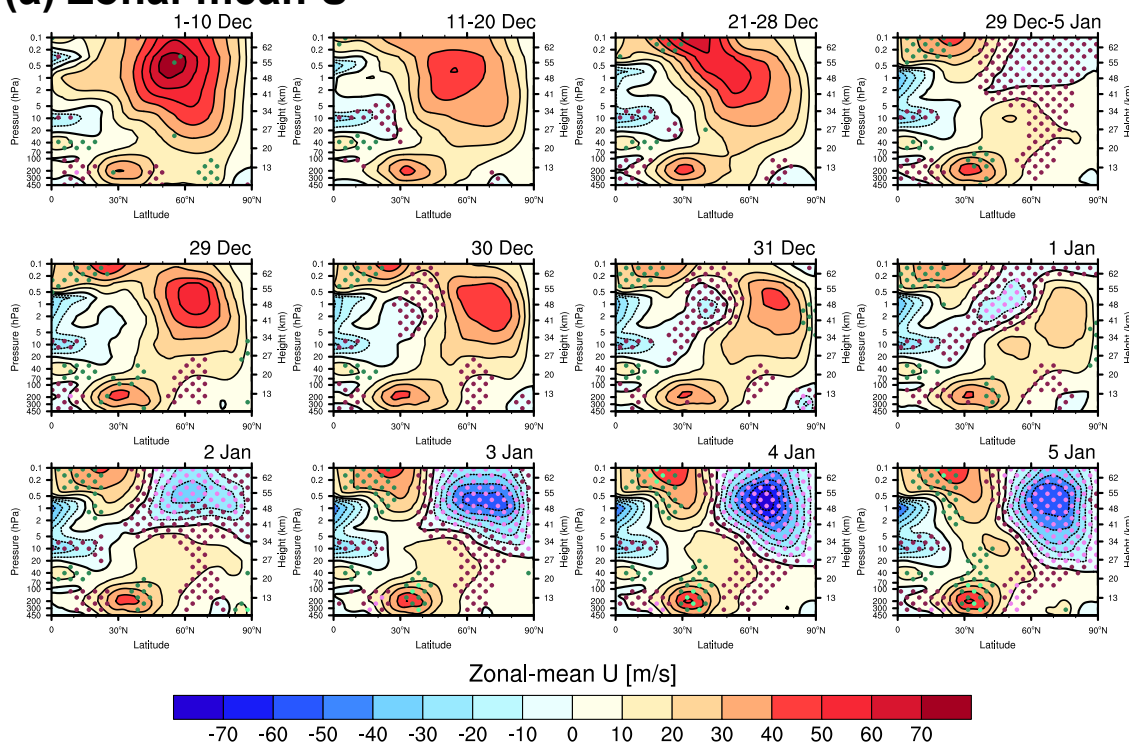


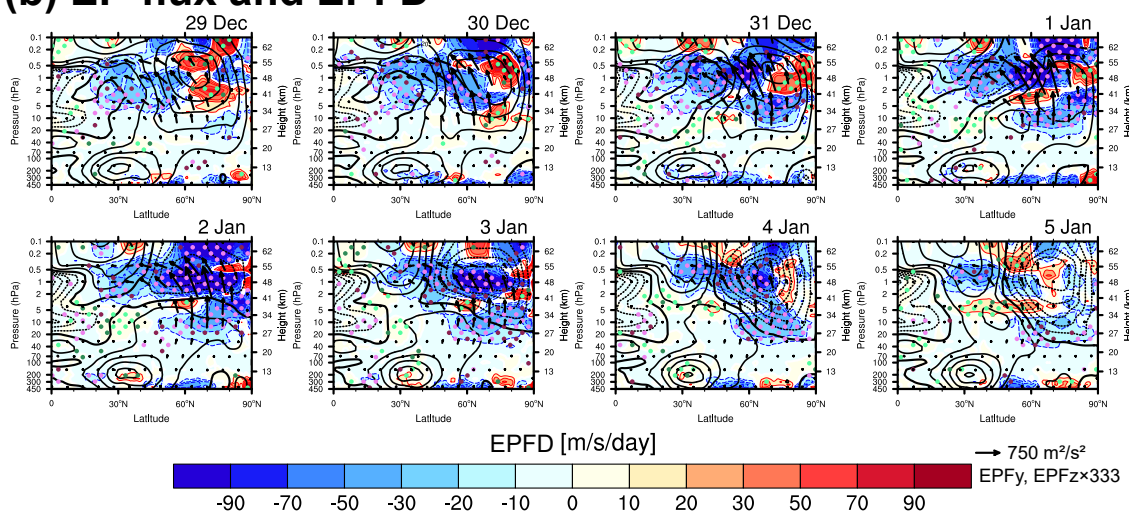
**Figure 6:** (a) Latitude-height cross sections of the zonal-mean magnitude of nonconservative forcing ( $Z'$ , shading) overlaid by the positive EPFD of PW2 (red contour) during 1–5 January 2021. The black contours present the zonal-mean zonal winds where the solid, dashed, and thick solid lines denote positive, negative, and zero wind, respectively. (b) Polar stereography series of  $Z'$  at 1 hPa altitude during the same period.



### (a) Zonal-mean U



### (b) EP-flux and EPFD



454

455 **Figure 7:** Latitude-height cross sections of (a) the zonal-mean zonal winds averaged over 1–10, 11–20, 21–28 December  
 456 2020, and 29 December 2020–5 January 2021 (first row), daily from 29 December 2020 to 5 January 2021 (second to  
 457 third row), and (b) EP fluxes (vectors) overlaid on the EPFD (colors) of the resolved waves. The black contours in (b)  
 458 are the zonal-mean zonal winds. The contour specifications are the same as in Figure 3.



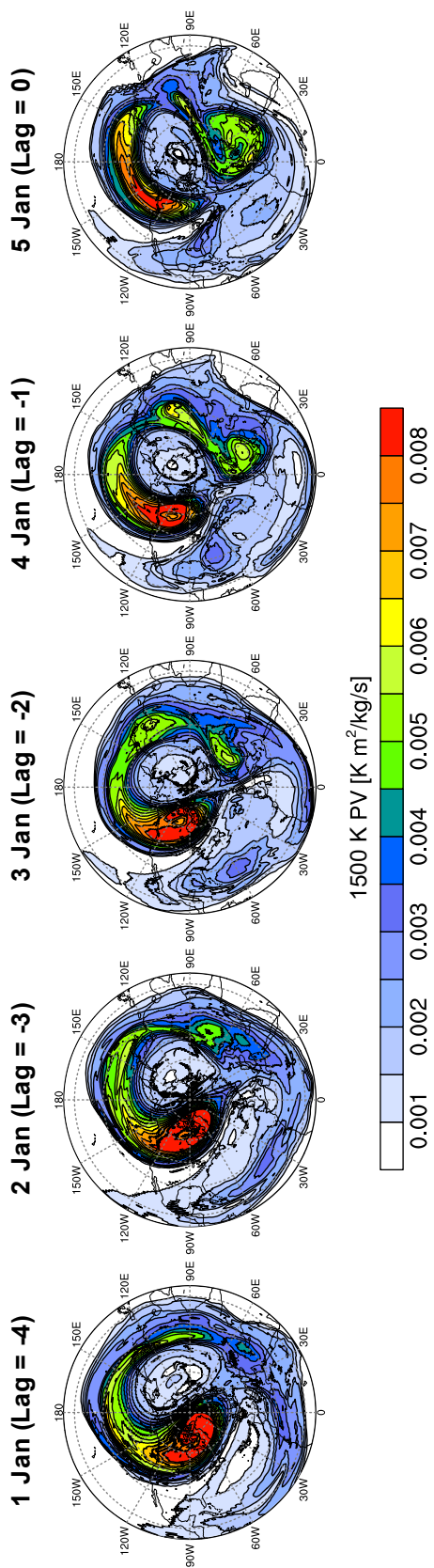


Figure 8: Time series of Ertel's potential vorticity at the 1500 K isentropic surface (~2 hPa).